Parametrically pumped electron oscillators

J. Tan and G. Gabrielse
Department of Physics, Harvard University, Cambridge, Massachusetts 02138
(Received 17 September 1992)

Parametrically pumped electron oscillators synchronize abruptly when the pump power exceeds a threshold and the oscillators are radiatively cooled in a cylindrical Penning trap. The collisionally coupled electron oscillators are under precise experimental control and exhibit a rich and varied nonlinear dynamics, with abrupt thresholds, hysteresis, abrupt transitions between bistable response phases, etc. Synchronized electrons are an ideal probe of the radiation field of a trap cavity, opening the way to a new generation of electron magnetic-moment measurements and to sideband cooling of an electron motion to millikelvin temperatures.

PACS number(s): 32.80.Pj, 05.40.+j, 12.20.−m

I. INTRODUCTION

In a recent Letter, we reported the discovery of self-organized collective motion of collisionally coupled electron oscillators which are parametrically pumped [1]. The oscillators are electrons suspended in a cylindrical Penning trap [2, 3] and their internal energy is controlled by varying their coupling to the radiation modes of the trap cavity. The use of the self-organized motion as a probe of the radiation field within the trap cavity, opening the way to a new generation of measurements of the magnetic moment of the electron and positron, is discussed separately in more detail [4]. Here we emphasize the simple observed features related to the cooperative behavior and nonlinear dynamics in coupled, parametric electron oscillators. Some of these can be understood with a simple model wherein the electrons oscillate rigidly together. Many others, however, are not yet understood despite the striking regularity in observed features which suggests an underlying simplicity. A more detailed description is available [5].

Related systems of coupled oscillators have been studied in recent efforts to characterize large dynamical systems which are far from equilibrium. Studies of the laser, for example, revealed that concepts and techniques of phase-transition theory can be generalized to this nonequilibrium system, providing a fruitful analogy to critical phenomena in a ferromagnet [6, 7]. Also, modest size arrays of Josephson-junction oscillators synchronize when they produce high-frequency microwaves, being coupled via a common load of passive circuit elements [8]. Large systems of well-characterized coupled oscillators are difficult to realize under good control in the laboratory. No unified theoretical approach has yet emerged for collective behavior far from thermal equilibrium. Nonetheless, an increasing number of studies with a few model systems of coupled limit-cycle oscillators are revealing recognizable cooperative phenomena such as oscillator synchronization, "clustering," and "attractor crowding" [9]. Examples include Van der Pol oscillators [10] and an "active rotator" model [11], which are theoretically studied using numerical solutions of coupled differential equations [10, 12, 13], using coupled iterative maps [14, 9], using generalized mean-field approaches [11], as well as using renormalization-group analysis [15].

Parametrically pumped electron oscillators are far from thermal equilibrium insofar as they are strongly driven and they continuously dissipate energy into a microwave cavity. A unique feature is that the oscillators synchronize to produce an observable, coherent motion of their center of mass (c.m.) at half the frequency of the pump. Time translation symmetry requires that any coherent response be bistable in phase relative to a subharmonic of the parametric pump. The collective motion is self-organized insofar as the choice between the bistable phases depends upon the internal motions of the electrons (not upon the external pumping field) and characteristically requires energy dissipation [16]. Transitions between the bistable phase states depend upon the internal energy of the oscillators (relative to their c.m.), reminiscent of a two-state system coupled to a thermal bath. This internal energy is varied by tuning the radiative dissipation to the cold trap cavity.

An important experimental feature of the electron oscillators in a cylindrical Penning trap is that numbers of electron oscillators, system nonlinearity, damping, etc., can be accurately controlled and varied. With a single-electron oscillator, the conditions can be so simplified that a most stringent test of QED can be made. With more oscillators, there is sufficient complexity to provide interesting and nontrivial nonlinear dynamics with features such as hysteresis, bistability, phase jumps, and thresholds. The precisely controlled system of electron oscillators remains manageable, nonetheless, offering the possibility to study in detail an activated barrier crossing in the collective motion of the parametrically pumped electron oscillators, for example.

The cylindrical trap cavity and the trapped electron oscillators are introduced in Sec. II. Parametric resonance of these oscillators is discussed in Sec. III, for the special case that internal electron motions are strongly cooled via a resonant coupling of electron cyclotron motion and a resonant radiation mode of the trap cavity. When the cyclotron frequency of the electrons is swept

through resonance with radiation modes of the trap cavity (Sec. IV), Lorentzian resonance line shapes are observed which make it possible to identify the standing-wave field configurations of the cylindrical cavity. Sidebands are observed due to the motion of the localized electrons through the standing waves and strong coupling (Sec. V) between the electrons and cavity also modifies the observed line shapes. Transistions between bistable phase responses are discussed in Sec. VI, and Sec. VII discusses the importance of fluctuations for the system of parametrically pumped electron oscillators. Throughout this work, we will switch between frequencies ν and the corresponding angular frequencies $\omega = 2\pi\nu$ as is convenient.

II. ELECTRONS IN A CYLINDRICAL PENNING TRAP CAVITY

This study of the collective behavior of parametrically pumped electron oscillators is made possible by the cylindrical Penning trap in Fig. 1, which is constructed to be the best possible approximation to an ideal microwave cavity. The cavity walls are split so that sections form the electrodes of a Penning trap in which only one electron or more than 10^4 electrons can be suspended and studied. Radiation modes of the trap cavity are clearly observed with resonant frequencies that correspond very well to the familiar eigenfrequencies of an ideal cylinder, as we shall see in Sec. IV. We will thus identify and classify the electromagnetic standing-wave fields in a familiar way as either transverse magnetic or transverse electric modes. Trapped electrons are thereby localized within well-characterized standing wave fields so that the interaction of the electrons with the surrounding radiation field is under precise control.

The familiar eigenfrequencies for a cylindrical microwave cavity of height $2z_0$ and radius ρ_0 (Fig. 2) are given by [17]

$$\omega_{mnp} = c\sqrt{\left(\frac{\chi_{mn}}{\rho_0}\right)^2 + \left(\frac{p\pi}{2z_0}\right)^2}, \tag{1}$$

where c is the speed of light. Transverse magnetic modes are designated by TM_{mnp} with χ_{mn} the nth zero of the mth-order Bessel function $J_m(x)$, and $p = 0, 1, 2, \ldots$ indicates the number of standing-wave nodes along the z axis. Transverse electric modes are designated by TE_{mnp} with χ_{mn} the nth zero of the Bessel function derivative $J'_m(x)$, and $p = 1, 2, \ldots$. In both cases, $m = 0, 1, \ldots$ and $n = 1, 2, \ldots$. The standing-wave fields are simple analytic functions which are readily available [17] so we do not display them here. With these analytic functions it is possible to calculate the interaction of particular cavity radiation modes with electrons localized in the trap cavity.

Standing-wave modes which couple to electron cyclotron motion (perpendicular to the axis of the cylinder) are of particular interest. An electric field perpendicular to the cylinder axis is required and is provided by both TE_{1np} or TM_{1np} standing-wave modes. Such modes with odd p have a maximum transverse electric field (antinode) at the center of the trap. Similar modes, except with even p, instead have a vanishing transverse electric field (node) at the center of the trap and hence do not couple to centered electrons. However, spatially displacing the electrons from antinode to node provides a way to rapidly couple and uncouple the electron and cavity, turning the cyclotron damping from on to off (Sec. IV). Moreover, the spatial gradients near the nodes are suited for sideband cooling thermal motions of electrons along the cavity axis (Sec. IV).

Anywhere from 1 to 10^5 or more electrons can be captured and localized within the cylindrical Penning trap cavity. The most stringent requirement upon the electrostatic potential V within the Penning trap is for the study of one trapped electron. An electrostatic quadrupole is required to produce a harmonic oscillation of the trapped particle, along the magnetic field direction $\hat{\mathbf{z}}$, at a well-defined and precisely measureable frequency ω_z which is independent of small amplitude variations. The potential

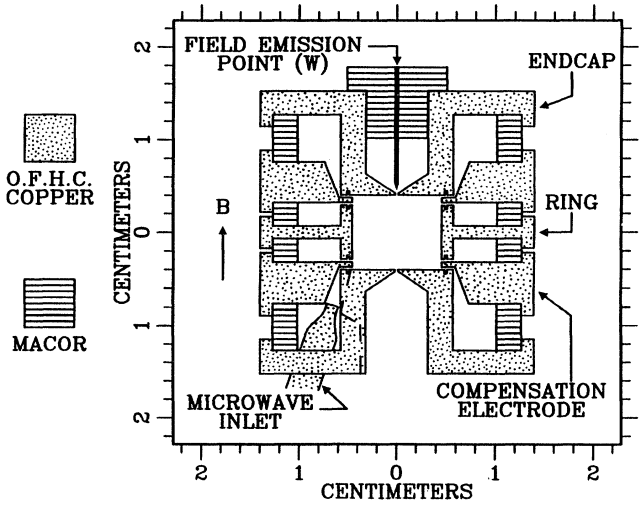

FIG. 1. Orthogonalized cylindrical trap cavity [to scale with $z_0 = 0.3838(6)$ cm and $\rho_0 = 0.4559(6)$ cm at 4 K]. A spatially uniform magnetic field ($\Delta B/B < 10^{-6}$ over $z_0/10$) is along the vertical axis.

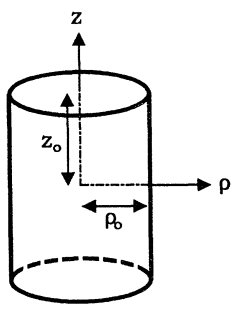

FIG. 2. Ideal cylindrical cavity.

can be written as

$$V = V_0 \frac{z^2 - \frac{1}{2}\rho^2}{2d^2}(1 + C_2) + \Delta V \tag{2}$$

where V_0 is the voltage applied to the electrodes, d is an appropriate trap dimension, C_2 is a dimensionless constant which depends upon the electrode geometry [2], and ΔV represents crucial corrections we shall discuss. The axial dimension z is the distance from the center of the trap and ρ is the corresponding radial coordinate. A particle of charge q and mass m oscillates at axial frequency ω_z given by

$$\omega_z^2 = \frac{qV_0}{md^2}(1 + C_2). \tag{3}$$

This axial oscillation frequency, at $\omega_z/2\pi = 63$ MHz, is precisely monitored, with small shifts in this frequency used to derive information about the cyclotron motion of the trapped electrons, for example.

Traditionally, an electrostatic quadrupole was produced using Penning traps with metal electrodes painstakingly shaped along the hyperbolic contours which are the equipotentials of the desired electrostatic quadrupole. We instead employ the cylindrical geometry so we can understand and control the radiation field in the trap cavity, but this is a much less straightforward way to produce a high-quality electrostatic quadrupole potential [a small ΔV in Eq. (2)]. The trap cavity has its vertical axis $\hat{\mathbf{z}}$ along the axis of a 6-T magnetic field from a superconducting solenoid. Small slits (0.015 cm) which incorporate choke flanges ($\lambda/4$ at 164 GHz) divide oxygen-free high-conductivity copper cavity walls into two end-cap electrodes (at z_0 above and below the trap center), a ring electrode (with radius ρ_0), and two compensation electrodes. The voltage applied to these compensation electrodes changes ΔV, with little change in the electrostatic quadrupole (i.e., in C_2) due to a judicious choice of the ratio ρ_0/z_0, which yields this crucial orthogonalization property [2]. The leading contributions to ΔV are given by

$$\Delta V = \frac{1}{2}C_4 V_0 \frac{z^4 - 3z^2\rho^2 + \frac{3}{8}\rho^4}{d^4} + \frac{1}{2}C_6 V_0 \frac{z^6 - \frac{15}{2}z^4\rho^2 + \frac{45}{8}z^2\rho^4 - \frac{5}{16}\rho^6}{d^6} \tag{4}$$

with C_4 tunable between $\pm 10^{-1}$, while C_6 remains relatively constant at $C_6 \approx -10^{-1}$. We are able to tune $|\ C_4\ | < 10^{-5}$ thereby making the axial oscillation of a single electron sufficiently harmonic so that the driven axial resonance in Fig. 3 is observed [3] with a signal-to-noise ratio fully as good as in hyperbolic Penning traps.

Once the potential is tuned optimally, the particle motions and particle detection of a trapped electron at the center of the trap is much the same in a cylindrical trap as in a traditional hyperbolic trap. Three familiar motions [18] include a cyclotron orbit around a magnetic field line (at frequency $\omega_c'/2\pi < 166$ GHz), the harmonic axial oscillation along the magnetic-field direction $\hat{\mathbf{z}}$ (at frequency $\omega_z/2\pi = 63$ MHz), and a circular magnetron motion (at a much lower 12 kHz frequency) which is not important for our purposes here. A tuned circuit attached to the trap electrodes damps and detects the axial motion of one electron, or the c.m. motion of more trapped electrons [20]. The circuit is kept near 4.2 K, as is the trap, by thermal contact to liquid helium. We learn about the collective motions of the trapped electrons from this signal.

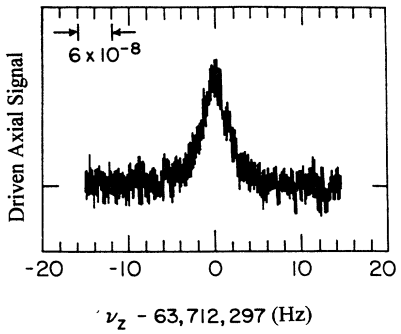

FIG. 3. Directly forced axial resonance of a single electron in a cylindrical Penning trap [3].

The driven axial resonance for a single electron in Fig. 3 is only 4 Hz wide. The width is the damping rate γ_z for a single electon. This rate is $(30\ \text{ms})^{-1}$ at maximum, but can be reduced by detuning the axial oscillation frequency from the resonant frequency of the tuned circuit. For the c.m. motion of $N > 1$ trapped electrons, the damping rate is $N\gamma_z$. Thus N is determined by the linewidth of the driven axial resonance (e.g., Fig. 4) divided by the corresponding linewidth for one electron (Fig. 3).

III. PARAMETRIC RESONANCE

Trapped electrons are driven parametrically by modulating the otherwise static voltage V_0 in Eq. (2) at fre-

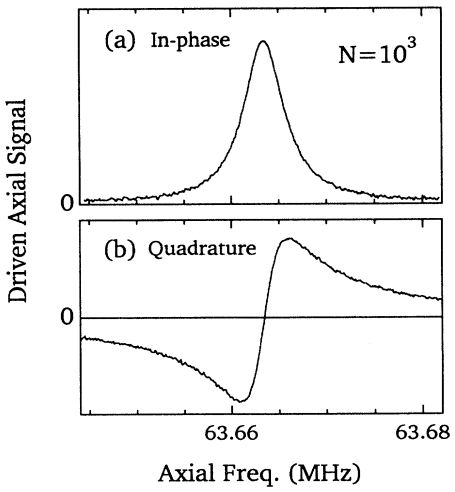

FIG. 4. Typical driven axial resonances of the center of mass of $N = 10^3$ electrons.

quency $\omega_d \approx 2\omega_z$. The spring "constant" for the axial restoring force becomes modulated

$$m\omega_z^2 \longrightarrow m\omega_z^2\,[1 + h\cos(\omega_d t)]\,. \tag{5}$$

Both the strength of the parametric drive h and its frequency ω_d are varied as part of these studies. The response of the center of mass of the trapped electrons, at frequencies near ω_z, is observed in much the same way [20, 21] as the driven signals in Figs. 3 and 4.

Figure 5 gives a simplified model. Trapped electrons are represented as oscillators on springs whose modulated spring constant has just been displayed. Trap electrodes are represented by the parallel conducting plates. We observe the current induced through the resistor R (representing a resonant tuned circuit) connected across the plates. Power dissipated in the resistor is responsible for the axial damping of the c.m., at rate $N\gamma_z$, which has been mentioned. The oscillatory voltage induced across R, proportional to the axial velocity of the c.m., is amplified and electronically processed to give the c.m. energy and the phase of the c.m. motion relative to the parametric pump. Because the pump is at twice the response frequency, time translation symmetry requires that any coherent, steady-state response of the electron's c.m. must have either of bistable phases that differ by 180°.

Throughout the rest of this section we confine our attention to the case where the cyclotron motion of the trapped electrons is coupled to a radiation mode of the trap cavity with which it is resonant. (Observed cavity modes are discussed presently in Sec. IV, in which case this restriction will be lifted.) Figure 6(a) shows that the energy in the axial c.m. motion abruptly increases by orders of magnitude as the strength h of the parametric pump is increased by less than 0.5 dB across a nonlinear threshold at $h = h_T$. Below this threshold, the axial c.m. motion is not detectably coherent with the subharmonic of the drive at $\omega_d/2$. (The coherence time is less than 1 ms.) Above threshold, however, the motion is phase coherent with the subharmonic of the drive. The coherence time is greater than 1000 s for $N > 2000$ electrons.

The pump strength at the sharp threshold h_T is measured to be proportional to the axial damping rate $N\gamma_z$ as shown in Fig. 6(b). The damping rate was varied by detuning the axial frequency ω_z from resonance with the tuned circuit that detects and damps the axial motion. The threshold h_T is separately proportional to the number of trapped electrons between $N = 60$ and 18 000 as shown in Fig. 6(c). By carefully measuring the strength of the pump voltage applied to the trap electrodes, we find that

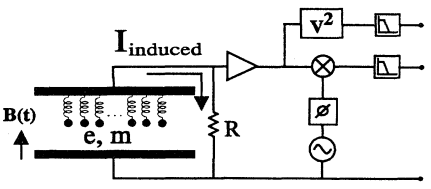

FIG. 5. Simplified detection diagram.

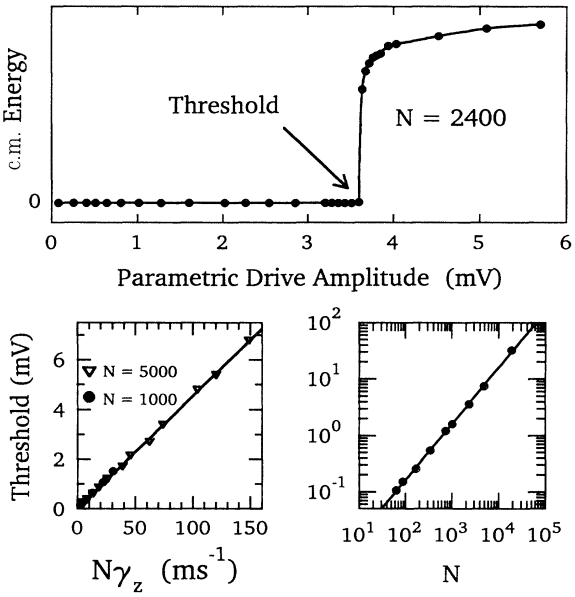

FIG. 6. (a) Observation of abrupt transition from weak, disordered motions to large, coherent c.m. oscillation at a pump strength threshold. Measured threshold varies linearly (b) with axial damping rate γ_z and (c) with the number of electrons N.

$$h_T = \frac{2N\gamma_z}{\omega_z}, \tag{6}$$

with the proportionality constant established to within 40%.

The measured threshold for the onset of parametrically excited motion in Eq. (6) is just the threshold which would be expected if the axial c.m. motion were the rigid motion of the N electrons. Such rigid motion is described by the differential equation

$$\ddot{Z} + (N\gamma_z)\dot{Z} + \omega_z^2[\,1 + h\cos(\omega_d t)\,]Z + \lambda_4 Z^3 + \lambda_4 Z^4 = 0. \tag{7}$$

Here $Z = \sum_i z_i/(Nd)$ is a dimensionless c.m. coordinate, with z_i/d the axial position of the ith electron scaled by the suitable trap dimension. The nonlinear terms, with strengths $\lambda_4 = 2C_4/(1+C_2)$ and $\lambda_6 = 3C_6/(1+C_2)$, arise from additions to a pure electrostatic quadrupole potential as has been discussed. For one electron ($N = 1$) exactly on the $\hat{\mathbf{z}}$ axis, this equation would be exact. As the drive strength h is increased through threshold in Eq. (6), solving this equation shows (in Fig. 7) that Z initially increases exponentially from $Z = 0$. The nonlinearities are not important near $Z = 0$ and hence do not influence the threshold strength h_T. However, as Z increases, the nonlinearities arrest the exponential growth and, together with the damping, establish a steady state amplitude for Z.

For small oscillations about $Z = 0$, before the onset of a large parametric oscillation, the rigid motion equation

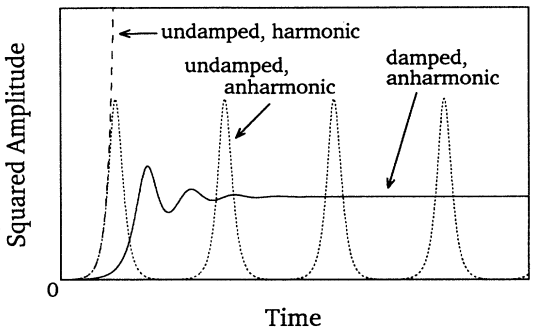

FIG. 7. Parametric resonance with characteristic exponential growth of harmonic oscillation (dashed line). Periodic variation results as anharmonicity arrests growth (dotted line), but damping causes relaxation to a steady state (solid line).

is just Mathieu's equation with damping. It is well known [22] that the $Z = 0$ solution to this equation is unstable in a region in ω_d vs h space which is bounded by a hyperbola (Fig. 8) and given by

$$-\frac{\sqrt{h^2 - h_T^2}}{2} < \frac{\omega_d - 2\omega_z}{\omega_z} < \frac{\sqrt{h^2 - h_T^2}}{2} . \qquad (8)$$

Any small fluctation triggers an excitation to large Z. As damping is reduced, the hyperbola approaches the dotted rays in the figure. For $\omega_d = 2\omega_z$ exactly, the figure shows that the threshold is at $h = h_T$ as already described.

By increasing the drive frequency, for a fixed drive strength $h > h_T$ and an initial condition $Z = 0$, we can further test this rigid model. Figure 9(a) shows observed line shapes in which parametric excitation is observed between frequencies ω_- and ω_+. Figure 9(b) shows the corresponding paths in ω_d vs h space. In Fig. 9(c) we plot the square of this excitation range $(\omega_+ - \omega_-)^2$ vs h^2. The straight line we observe indicates the hyperbolic boundary of the instability region anticipated in Eq. (8) above.

The line shapes for parametric excitation, unlike the frequency range of instability just discussed, depend upon the nonlinearities (upon the particular values of λ_4 and λ_6). Figure 10 shows observed line shapes. The

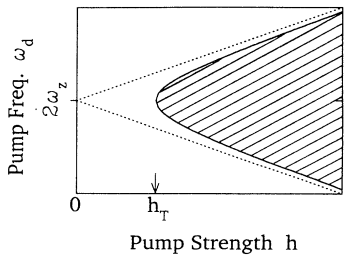

FIG. 8. Instability region (shaded) for a solution to Mathieu's equation with damping (solid hyperbola). Without damping, the instability region would be instead bounded by the dotted rays.

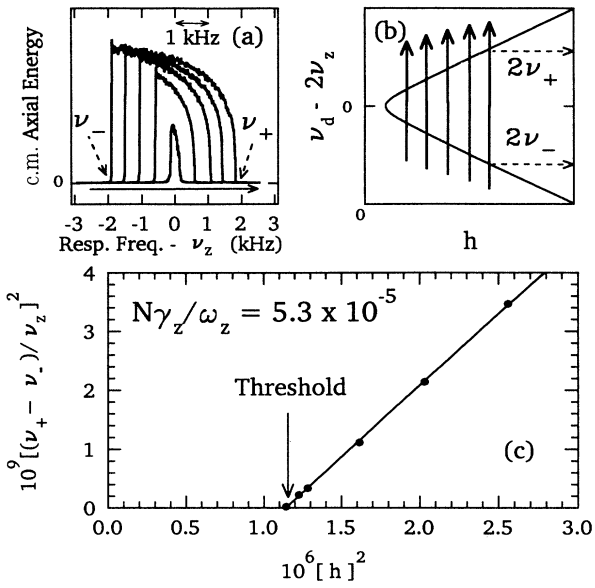

FIG. 9. Observed frequency range of instability (a) increases with h. Increasing ω_d at fixed h values, as illustrated in (b), generates this family of parametric resonances. Measured corner frequencies $\nu_+(h)$ and $\nu_-(h)$ fit well to a hyperbola (c) when plotted versus h^2.

axial c.m. energy is plotted versus the parametric pump frequency for a pump strength $h = 1.3h_T$. A linear line shape is observed when C_4 is deliberately made large enough so this nonlinearity dominates [Fig. 10(a)]. When $|C_4|$ is minimized, so the C_6 nonlinearity dominates, a different characteristic shape is observed [Fig. 10(b)]. These shapes are also obtained from the steady-state solutions [5] to the differential equation Eq. (7). For dominant C_4,

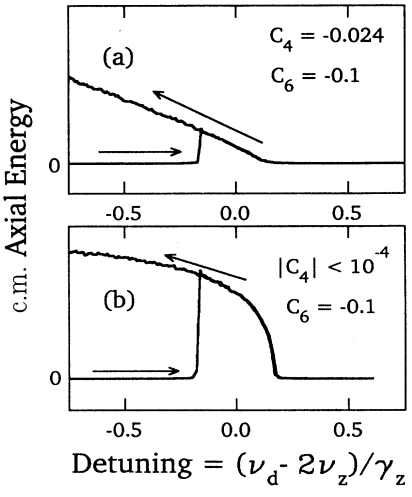

FIG. 10. Observed resonance line shapes with hysteresis. Maximum c.m. energy is limited by cavity cooling but line shapes (a) for large C_4 and (b) for negligible C_4 agree qualitatively with rigid model.

excited steady states have amplitude given by

$$A^2 = \frac{4}{3}\frac{1}{\lambda_4}\left[\frac{2(\Omega-\omega_z)}{\omega_z} \pm \frac{1}{2}\sqrt{h^2-h_T^2}\right], \quad (9)$$

where the sign for stable solutions depends on the anharmonicity [e.g., the minus sign is chosen if $\lambda_4 < 0$, as in Fig. 11(a)]. For dominant C_6, nontrivial steady-state solutions have

$$A^4 = \frac{8}{5}\frac{1}{\lambda_6}\left[\frac{2(\Omega-\omega_z)}{\omega_z} \pm \frac{1}{2}\sqrt{h^2-h_T^2}\right], \quad (10)$$

with the same sign selection rule [e.g., Fig. 11(b)]. In both the observed and calculated line shapes there is hysteresis. When the pump frequency is swept down for fixed pump strength the large excitation persists even after the pump frequency drops below ω_- because the effective resonant frequency is shifted by the large excitation. Hysteresis is also observed (Fig. 12) when the pump frequency is fixed and the pump strength is swept back and forth through the region of instability (more details in Ref. [5]).

The observations discussed in this section are all consistent with a parametric excitation of the rigid motion of N trapped electrons. In the following sections, however, we shall see that more detailed observations do not conform to this simplified model.

IV. CAVITY MODE RESONANCES

We now relax the requirement of Sec. III that the cyclotron motion of trapped electrons be resonant with a radiation mode of the trap cavity. The parametric drive is fixed at frequency $\omega_d = 2\omega_z$ and strength of about $h = 1.3h_T$ (i.e., 2 dB above threshold), while the magnetic field is swept to bring the cyclotron frequency of

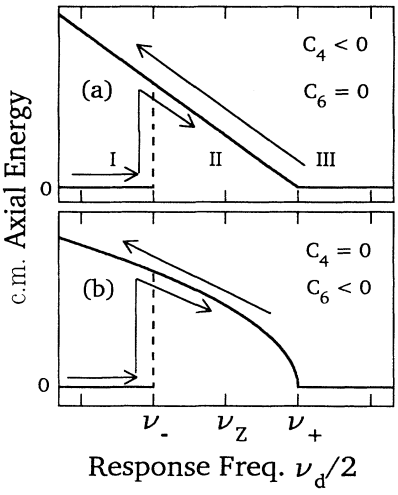

FIG. 11. Calculated rigid model line shapes, showing hysteresis of c.m. energy versus pump frequency ν_d. c.m. energy is (a) a linear function of pump frequency ν_d for $C_4 < 0$ with $C_6 = 0$, and (b) a parabolic function of ν_d for $C_4 = 0$ with $C_6 < 0$.

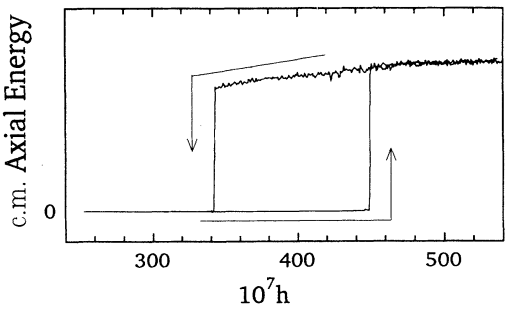

FIG. 12. Example of observed hysteresis loop when pump strength is increased from below threshold into the instability region and then decreased below threshold, with fixed pump frequency.

the trapped electrons into resonance with one mode after the other. Figure 13 shows the experimental setup. The axial center-of-mass energy is monitored as a function of solenoid current, which is equivalently calibrated in terms of magnetic-field strength and electron cyclotron frequency. The magnetic field is provided by a superconducting solenoid designed for precision NMR experiments. The cyclotron frequency is slowly swept into resonance with the cavity modes by ramping the current in the superconducting solenoid ($\sim$ 200 H). The current in the solenoid and the signal from the electron oscillators are digitized simultaneously and stored in a computer. A conversion from measured solenoid current to cyclotron frequency is obtained by exciting a cyclotron resonance with a microwave source at a high field.

Figure 14(a) illustrates the great sensitivity of the

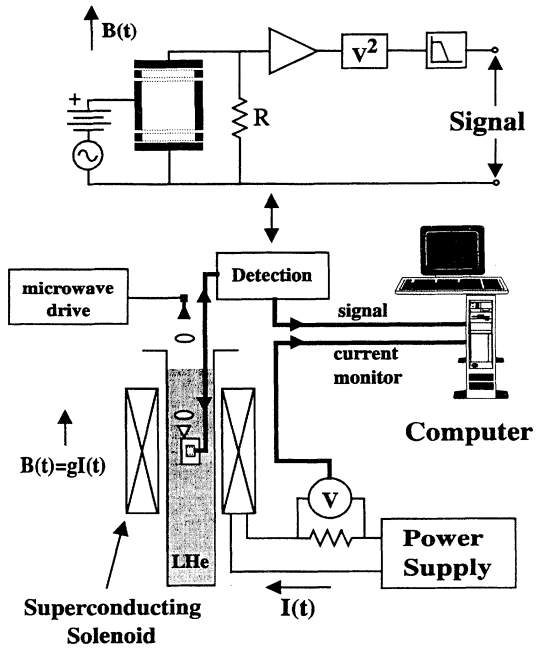

FIG. 13. Simplified diagram of the experimental apparatus for cavity-mode detection.

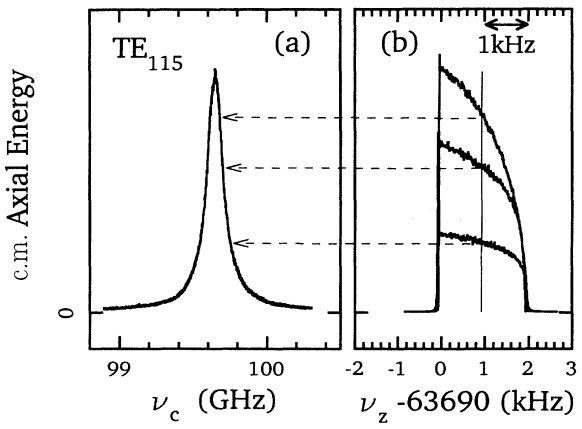

FIG. 14. (a) Cavity resonance observed by monitoring the axial c.m. energy while slowly sweeping the magnetic field to vary ω_c', with pump frequency at $\omega_d = 2\omega_z$ and pump strength $h = 1.3h_T$. (b) Parametric axial resonances for indicated cyclotron frequencies as the parametric pump frequency is swept through $\omega_d \approx 2\omega_z$ while the response at $\omega_d/2$ is monitored.

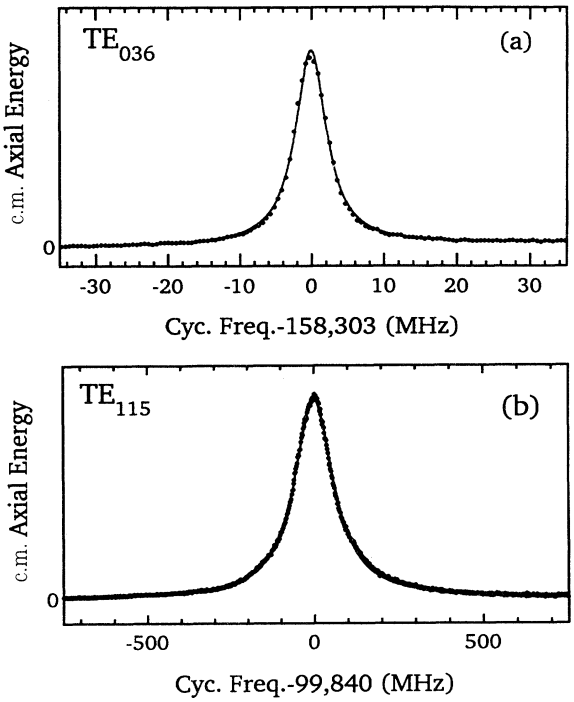

FIG. 15. Lorentzian line shapes (solid lines) fit to observed cavity modes (dots) which are well separated from other modes.

parametric resonance at $2\omega_z$ to resonance between the cyclotron frequency ω_c' and eigenfrequencies of radiation modes of the trap cavity. In Fig. 14(a), the axial c.m. energy rises as the electron cyclotron frequency ω_c' is swept continuously through resonance with the TE_{115} mode. Figure 14(b) shows in more detail how this comes about for the three indicated detunings between ω_c' and ω_{115}. The parametric resonance line shape at each detuning has the same ω_-, ω_+ and characteristic shape discussed earlier, but the level of excitation clearly depends upon the detuning.

The strongest observed signals (i.e., largest areas) correspond to TE_{1np} and TM_{1np} modes with p odd. These modes couple most strongly to electron cyclotron motions owing to a nonvanishing transverse electric field at the trap center and some such modes have quality factors as high as $Q = 10^4$. An extremely fortunate feature, not yet understood, is that isolated cavity mode resonances such as Fig. 14(a) typically fit very well to a Lorentzian line shape as illustrated in Fig. 15. We would expect a rise in axial c.m. energy at resonance, on the assumption that the increased cyclotron damping removes internal energy from the electrons and thus keeps nonlinearities sampled by the internal motions from disrupting the rigid c.m. motion described by Eq. (7). Why the rise is Lorentzian is not clear. Nonetheless, the line shapes and widths remain constant as the pump strength and number of electrons is varied over a wide range. In what follows, the measured resonant frequencies and Lorentzian linewidths are therefore assumed to be properties of the radiation modes of the trap cavity.

The extraordinary sensitivity of the synchronized motion of the electron oscillators to radiative cooling (an energy transfer to the modes of the trap cavity) allowed us to observe even weakly coupled cavity modes which have nodes in the midplane. For modes with standing-wave nodes at the trap center, the electron cloud experiences a microwave field that is amplitude modulated by its driven motion at $\omega_d/2 \approx \omega_z$. Such modes (e.g., those mentioned above except with p even) thus produce two Lorentzians split by ω_d as illustrated in Fig. 16(a). One peak is seen again when we apply a dc offset potential to the electrodes to shift the electron cloud along the magnetic field by $\lambda/4$ to an antinode of the standing wave field [4]. (Such studies suggest that the cloud size is at least less than $z_0/10$.) The motional effect is different (and typically smaller) for p odd modes since they have an antinode at the trap center. Nevertheless, for sufficiently large oscillations and for large p, small sidebands are observed at $2\nu_z$ on either side of the strong central peak as illustrated in Fig. 16(b).

With motional effects understood, the observed cavity modes of a Penning trap are identified with familiar standing-wave field configurations, as illustrated in Fig. 17. Over 100 cavity modes are observed [4, 5] over a very broad frequency range by sweeping ν_c' from below the lowest cavity mode at 26 GHz up to 166 GHz, by changing the magnetic field between 0.8 T and the solenoid's maximum rated field of 5.9 T. Thermal cycling of the trap apparatus up to 300 K and back to 4.2 K changes the observed resonance frequencies by less than 0.1%. The modes are identified as transverse electric TE_{mnp} or transverse magnetic TM_{mnp} using resonant frequencies which correspond well to those calculated for a perfect cylindrical cavity [17]. For example, the azimuthally symmetric TE modes with $m = 0$ have high-Q values and are not shifted much by the slits because induced surface currents flow parallel to the slits, allowing the trap cavity dimensions to be determined *in*

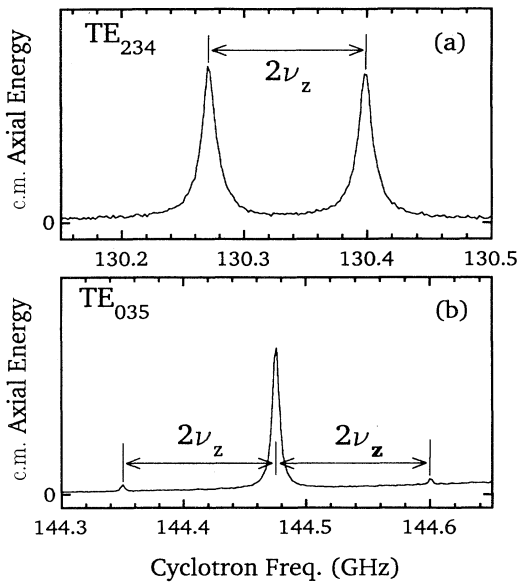

FIG. 16. (a) Motional doublet for a mode with p even has separation of $2\nu_z$. (b) For a mode with odd p, small sidebands are separated from the strong central peak by $2\nu_z$.

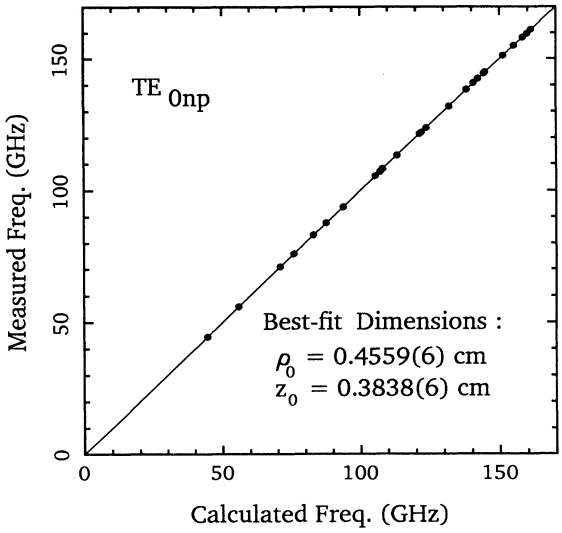

FIG. 18. Fit of measured TE_{0np} mode eigenfrequencies to those calculated for an ideal cylinder, *in situ* at 4 K, determines effective dimensions of the trap cavity to within 6 μm.

situ at 4 K to within 6 μm, as shown in Fig. 18. Calculated and measured mode frequencies for other modes of interest agree typically to a percent or better (Fig. 19).

Synchronized electrons allow the identification of the radiation modes of a trap cavity, and this should prompt a new generation of electron magnetic-moment measurements. These important measurements provide the most accurate comparison of theory (quantum electrodynamics) and experiment for an elementary particle and have alternatively provided the most precise value for the fine-structure constant. Past measurements [23] employed hyperbolic Penning trap cavities whose microwave properties were almost entirely unknown experimentally and whose resonant modes have only been crudely calculated numerically [24]. A cavity-modified spontaneous-emission rate for one electron in a hyperbolic trap cavity first focused attention upon these problems [25], and a "bolometric technique" later added evidence for some sort of modes in another hyperbolic cavity [21]. However, no mode was identified by its field symmetries and it remains unknown whether the observed modes of traps used for these precision experiments even couple to a single electron at their center. Moreover, the Q values quoted are only estimates given that Lorentzian line shapes were not established. The largest error assigned [23] was thus based on calculated frequency shifts for a

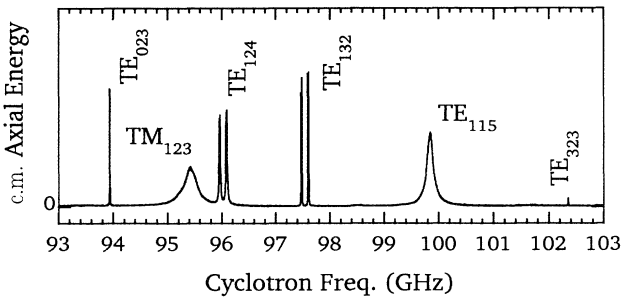

FIG. 17. A small slice of the cavity mode spectrum (taken in 34 min) with a signal proportional to energy in the axial c.m. motion. A full spectrum is in [4] and [5].

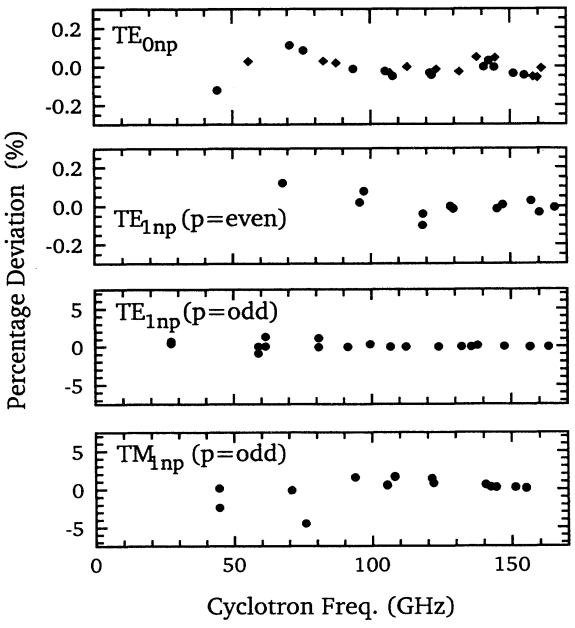

FIG. 19. Comparison of observed and calculated eigenfrequencies for series of cavity modes of particular experimental interest.

cylindrical trap model [24] of unknown applicability.

In the well-characterized radiation field of a cylindrical Penning trap, cyclotron damping and frequency shifts can be systematically studied as a function of detuning of the cyclotron frequency from the resonant frequency of identified modes. Comparisons with simple theoretical forms [4, 24] (appropriately corrected for renormalization effects) should be possible because the field symmetries are well known. In addition, the intense microwave gradient field built up in a high-Q mode with p even and $m = 1$ should allow sideband cooling [26, 18] at $\omega_c' - \omega_z$ of undamped axial motion (uncoupled from the LCR circuit) to millikelvin temperatures [27]. This temperature would be 10^3 times lower than previously achieved with an elementary particle. These same modes have a transverse magnetic field at the cavity center that could directly flip an electron spin without exciting cyclotron motion.

V. STRONG COUPLING

Isolated modes fit well to Lorentzian line shapes, as has been illustrated. Non-Lorentzian line shapes are also observed when an electron cloud and a cavity mode are strongly coupled. To illustrate the line-shape modification, Fig. 20(a) shows the observed resonance for TE_{115} which fits well to a Lorentzian line shape, with small number of electrons. The number of electrons is increased in Fig. 20(b), resulting in broadening of the line, especially at its base. With further increase in trapped electrons, the observed resonance is split, as shown in Fig. 20(c).

For weak coupling, the decay rate of one cyclotron oscillator to the Mth cavity-mode is given by

$$\gamma = \frac{\gamma_M}{1+\delta^2}, \tag{11}$$

where δ is the detuning between the cyclotron and cavity-mode resonant frequencies. A useful parameter for comparing the coupling time between the c.m. cyclotron motion of N electrons and a cavity mode, on the one hand, to the decay rate of the standing wave itself due to losses in the cavity walls, on the other hand, is defined by the ratio of these coupling rates

$$\eta = \frac{N^2\gamma_M}{\Gamma_M}. \tag{12}$$

The numerator gives the rate of energy transfer from the c.m. cyclotron motion to the Mth cavity mode. It is proportional to N^2 because this rate depends on the square of the charge of the oscillator. The denominator Γ_M gives the rate of energy from the cavity mode due to losses in the cavity walls. The weak-coupling approximation, which provides Eq. (11), is valid when $\eta \ll 1$. We rewrite η defined in Eq. (12), as

$$\eta = \frac{4}{3}\left[\frac{\gamma_M}{Q_M\gamma_c}\right] N^2 Q_M^2 \left(\frac{r_e\omega M}{C}\right) \tag{13}$$

in terms of known quantities (from calculations and measurements), with r_e being the classical electron radius and γ_c being the decay rate of one electron in free space. The factor in square brackets is calculable, depending only on the geometry of the cavity. It is tabulated in Ref. [5] for the trap in Fig. 1. The coupling increases in proportion to the square of N and the square of Q. By making N and Q sufficiently large, the coupling time for the cloud and a mode can be shorter than the decay time for the cavity mode itself $\Gamma_M = \omega_M/Q$. Under this strong-coupling condition, the weak-coupling approximation breaks down because the c.m. cyclotron oscillator and the cavity mode can form normal modes. For TE_{115}, we observed that $\nu_M = 99.84$ GHz and $Q_M = 690$ in the weak-coupling limit, and therefore

$$\eta = 6.51 \times 10^{-8} N^2. \tag{14}$$

With 700 electrons, $\eta = 0.03$, a Lorentzian line shape is observed, consistent with Eq. (11). Broadening of the line shape is observed when $N = 2 \times 10^4$, which corresponds to $\eta = 25$. Evidence of normal-mode splitting is obtained when the number of electrons is increased to $N = 10^5$, corresponding to $\eta = 650$. Normal-mode splitting has been observed recently in other systems with atoms coupled to a cavity mode as an atomic beam passes through a high-finesse optical cavity [28, 29].

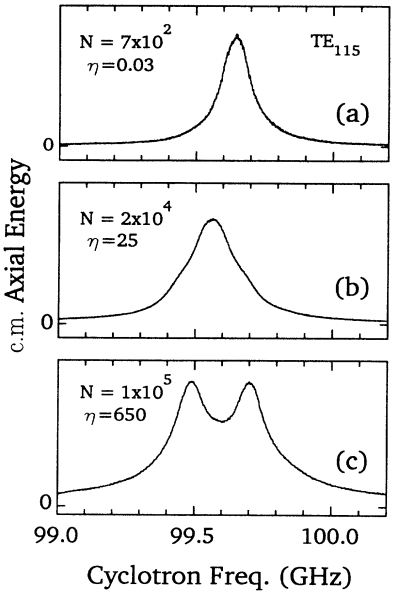

FIG. 20. The Lorentzian line shape (a) is modified to the strongly coupled line shapes in (b) and (c) as the number of electron N is increased to increase the electron-cavity coupling.

VI. TRANSITIONS BETWEEN PHASE-BISTABLE STATES

A coherent response of a system which is driven at twice the response frequency can with equal likelihood have either of steady-state phases which differ by 180°. An electronic signal proportional to $\cos(\chi)$ is observed, from phase sensitive electronics as in Fig. 5, where χ

is the phase difference between the phase of the axial center-of-mass motion and an oscillator which oscillates at exactly half of the frequency of the parametric pump. A change from one bistable oscillation phase to the second (displaced by 180°) thus corresponds to a change in sign in the observed electrical signal. The signal is also proportional to the amplitude of oscillation.

We observe abrupt transitions between the two phases, as illustrated in Fig. 21. These transitions appear to be similar to those attributed to a much poorer vacuum in an earlier experiment with only one electron [19]. Based upon antiproton measurements in a similar apparatus [30], however, we expect our pressure is below 5×10^{-17} Torr so that collisions are entirely irrelevant to these observations. Thousands of flips observed over many hours produce the distribution of time between flips τ, illustrated in Fig. 22 for $N = 750$ electrons. The distribution of times between flips is exponential, indicating the flips are random over all but the shortest times. However, there is a distinct "overabundance" of short residence times. In Fig. 22(a), more than 30% of the observed transitions occur during the first 5 s of the 50-s time bin.

A close look at the transitions themselves reveals a diversity of jump "trajectories," as illustrated in Fig. 23 for identical $N = 700$ electrons. In many cases [e.g., Fig. 23(a)], the c.m. motion first collapses for a period which can be as long as 100 ms, and then the transition is completed. In some cases a transition is preceded by a period of increased fluctuations [Fig. 23(b)]. In other cases [Figs. 23(c)–23(e)], completion of a transition takes several attempts in rapid succession. Figure 23(f) shows a rare event in which the c.m. motion appears to be oscillating unabated between the "basins" of two phase states. The duration of the transitions τ_J defined loosely in Fig. 23(a), has a distribution between 10 and 100 ms

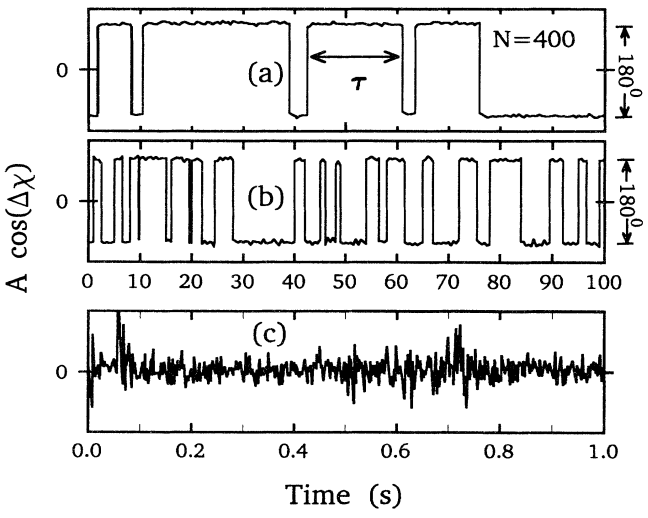

FIG. 21. (a) and (b) Random transitions between phase-bistable states. (b) The mean residence time $\bar{\tau}$ on average becomes shorter with increasing detuning between cyclotron and cavity mode frequencies. Disordered motion (c) results if cyclotron cooling is weak.

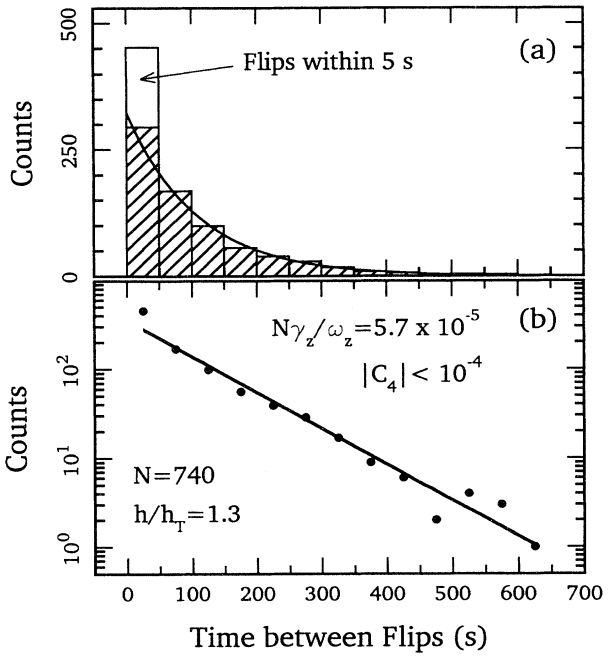

FIG. 22. (a) Distribution of residence times and (b) a fit to an exponential form.

depending upon pump strength, anharmonicity, number of electrons, etc., as illustrated in Fig. 24(b).

The mean time between transitions (or mean residence time) $\bar{\tau}$ varies greatly when system parameters are changed. It increases rapidly with the number of electrons N since the fluctuating motions of a larger number of electrons average to a smaller sized fluctuation of their c.m. motion [Fig. 25(a)]. For $N > 2500$, no transition is observed over hours when ω_c' is resonant with a cavity mode such as TE_{115}. The mean residence time is also observed to be longer for larger C_4 [Fig. 25(b)], apparently because a more anharmonic trap reduces the internal energy. The internal energy may be lower because the amplitudes of desynchronized oscillations are smaller and the cooling of internal oscillations via the LCR circuit is more efficient with larger anharmonicity. The switching rate increases rapidly with increasing internal energy. Consistent with this interpretation, an increase in the pump power [Fig. 25(c)] or a stochastic modulation of the spring constant ω_z^2 (by applying a broadband noise potential to the ring) diminishes the mean residence time. The internal energy is conveniently controlled via the electron-cavity interactions. Figure 25(d) shows the rapid decrease in mean residence time $\bar{\tau}$ for a cloud of $N = 400$ electrons as the frequency ω_c' is detuned from resonance with the TE_{115} cavity mode in Fig. 17). Transitions occur least frequently very near to resonance with a cavity mode [Fig. 21(a)] where the internal motion is most strongly cooled. The switching rate $\bar{\tau}^{-1}$ increases [Fig. 21(b)] when a slight detuning of ω_c' from the mode resonance allows the internal energy to rise. As the decreasing residence times τ become comparable with the phase jump times τ_J, the c.m. motion becomes "tur-

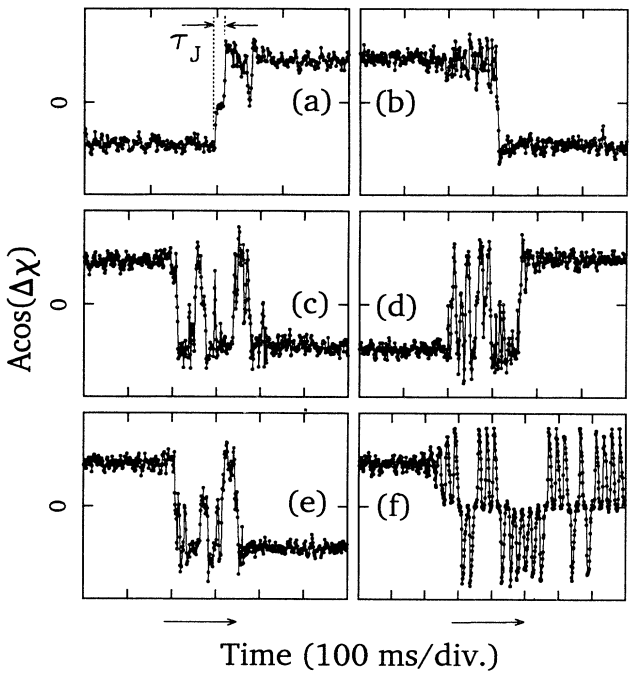

FIG. 23. Examples of phase jump "trajectories" observed with 600 electrons parametrically pumped at $h = 1.4h_T$, with $C_4 \sim -6 \times 10^{-4}$ and $N\gamma_z/\omega_z = 1.2 \times 10^{-5}$.

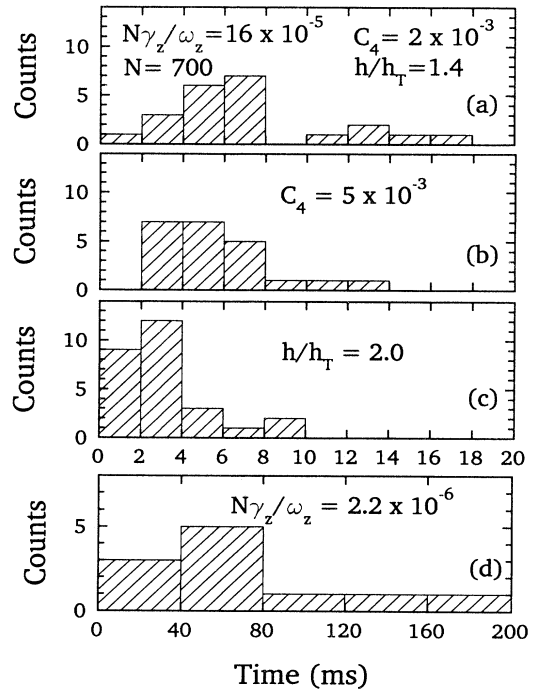

FIG. 24. Distribution of jump times and variation with control parameters. In (b)–(d), only the changed control parameter with respect to (a) is noted.

bulent." The observed signals of the two phase states are lowered and punctuated by random periods of incoherence. Further off resonance [cross-hatched region in Fig. 25(d)], the internal energy increases sufficiently so that the random, desynchronized motions of the electrons keep a detectable coherent c.m. motion from developing [Fig. 21(c)] because of the nonlinear couplings.

VII. FLUCTUATIONS AND RELATED PHENOMENA

The simplicity of a rigid model facilitates insight into the collective behavior of parametrically pumped electron oscillators. As we have seen, however, this model cannot explain the Lorentzian line shapes of observed cavity-mode resonances, why the parametric axial resonance is at all sensitive to resonant cyclotron damping by the cavity modes, or the random transitions between the phase-bistable states. Even when cavity cooling of internal motions is maximized, there is more interesting non-rigid behavior, which we now survey.

Near threshold ($h \approx h_T$, $\omega_d = 2\omega_z$), the character of the quiescent state changes rather dramatically with small change in the pump strength. Fluctuations in the c.m. motion grow as the pump strength increase toward the threshold, as shown on magnified scale in Fig. 26(a), but the coherence time remains short. To observe fluctuations in the signal directly, a storage scope captures the amplified i.f. signal, externally triggered by a precision frequency synthesizer at the same frequency and is coherent with the parametic pump. Fluctuations persist above the threshold in the partially coherent c.m. motion, with observable deviations [dotted lines in Fig. 26(b)] from a mean coherent oscillation [solid line in Fig. 26(b)] and interesting consequences for this phase-bistable system, as already discussed. Both coherent and stochastic components of the c.m. motion are examined in more detail using a spectrum analyzer to observe the Fourier distribution of signal. The electron oscillators are pumped by a frequency synthesizer with very high spectral purity, suitable for high-precision radio-frequency spectroscopy. We study changes in the response spectrum brought about by varying a system parameter. In Fig. 27, the magnetic field is changed, to detune ω_c' from resonance with a cavity mode by a detuning of δ, to control the radiative cooling of internal motions. The Fourier spectrum of the response above threshold consists of a broad "pedestal" due to fluctuations and a sharp peak which is orders of magnitude stronger due to the coherent motion. The fluctuation spectrum spectra are averaged over 100 samples. The highest three points in Fig. 27 (log-linear plot) shows the coherent component at $\nu_d/2$ decreasing as the internal energy is increased by detuning the ω_c' from a cavity mode. The spectrum of the fluctuations broadens with increasing detuning from a cavity mode (i.e., increasing internal energy).

The threshold of instability h_T is observed to be independent of internal energy, as illustrated in Fig. 28 (obtained by sweeping the pump strength for the identical detunings used in Fig. 27), except for a small fluctuation at the 1% level. The energy in the coherent c.m. motion

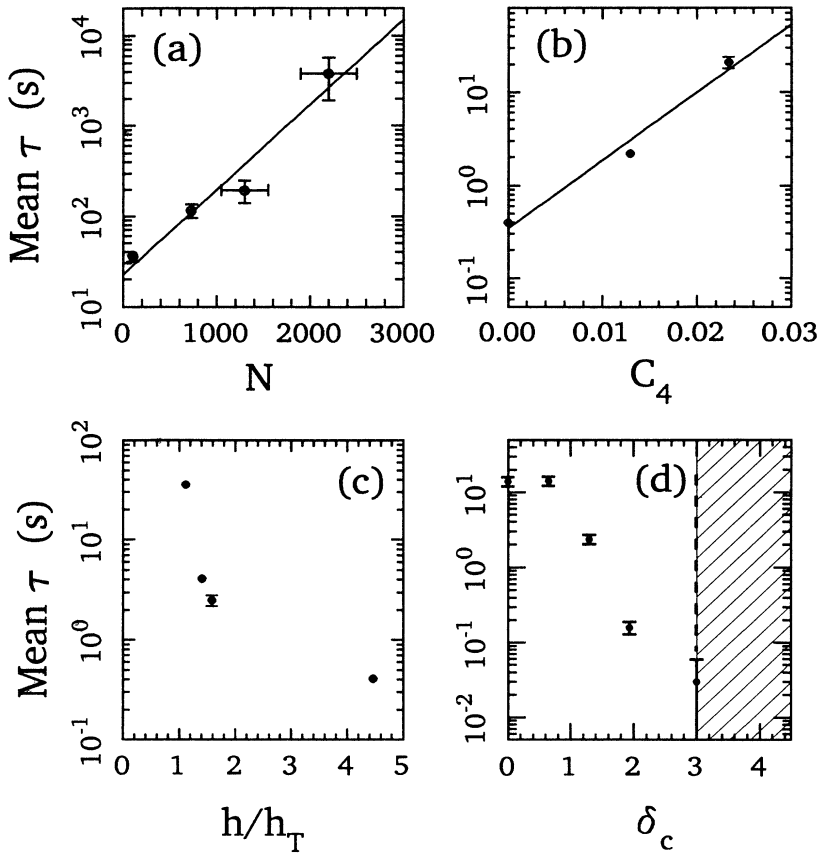

FIG. 25. Dependence of mean residence time $\overline{\tau}$ on control parameters. Mean time between phase flips versus (a) number of electrons N, (b) anharmonicity coefficient $|C_4|$, (c) pump strength h, and (d) detuning between cyclotron frequency and a cavity-mode eigenfrequency δ_c.

increases as the cyclotron frequency is tuned closer to the cavity eigenfrequency (for TE_{115}). It is noteworthy that Fig. 28 shows less noise in the measured mean-squared amplitude for larger detunings from the cavity mode. It appears that the frequency spectrum broadens but amplitude noise is reduced when the cyclotron frequency is detuned from cavity-mode resonance. A more detailed study of the amplitude and phase fluctuation as a function of cavity cooling would be interesting.

The limitations of the rigid model become obvious again, even when the radiative cooling of internal motions is maximized. With the electrons resonantly cooled by the mode TE_{115}, the Fourier spectrum is observed to change dramatically with increasing pump strength, as shown in Fig. 29 (each spectrum is an average of 100 samples). Only the broad, fluctuation spectrum is present below threshold [Fig. 29(a)]. The observed width is of order $N\gamma_z/2\pi$ but becomes narrower as the pump strength approaches the threshold. When the pump strength exceeds h_T, a sharp peak [much narrower than the detection bandwidth of 5 Hz in Fig. 29(a) and 25 Hz in Fig. 29(b)] emerges from a larger pedestal. The pump strength is increased first in increments of +1 dB in Fig. 29(a) and then in increments of +2dB in Fig. 29(b). The fluctuation spectrum broadens as the pump strength increases and is skewed for high pump strengths [Fig. 29(b)].

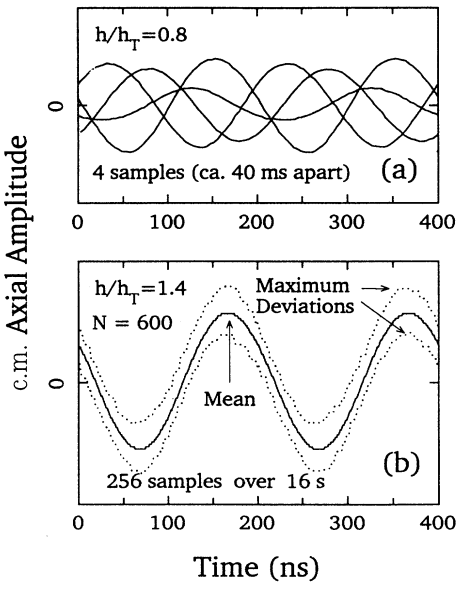

FIG. 26. Sampled IF signal illustrates (a) incoherent response for $h < h_T$ and (b) long-term coherence for $h > h_T$. Dotted lines in (b) show maximum deviations from mean coherent response (solid curve).

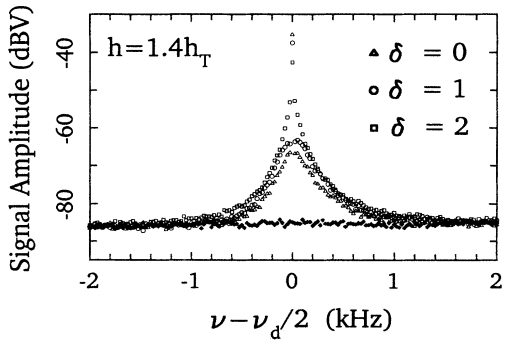

FIG. 27. Fourier spectra of responses for various detunings from a cavity mode. Coherent response (peak in a single channel) diminishes as cyclotron frequency is detuned from cavity-mode eigenfrequency, but fluctuation spectrum broadens.

Figure 30 shows the power in the peak (squares) and the integrated power in the fluctuation spectrum (circles) versus pump strength for the data set shown in Fig. 29. The integrated power of the fluctuation spectrum is the sum of contributions from each frequency bin with the white-noise background subtracted and the peak removed by omitting the central bin. Above threshold, the coherent component grows with pump strength but saturates at $h \approx 1.6h_T$ and slowly decreases for $1.6h_T < h < 6h_T$. This is an important disagreement with the rigid model, which predicts the c.m. energy to be a monotonically increasing function of the drive strength. For example, if the leading anharmonicity λ_4 is dominant, then the squared amplitude of the steady-state rigid motion goes as

$$A^2 \propto \sqrt{h^2 - h_T^2} \tag{15}$$

when the drive frequency is $\omega_d = 2\tilde{\omega}_z$. On the other hand, Fig. 28 shows that observed energy in coherent c.m. motion is limited by cooling via radiation into the cavity, as well as by anharmonicity as would be expected

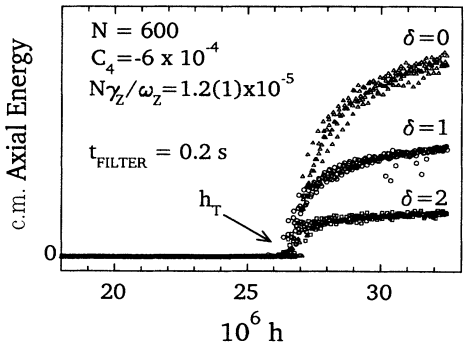

FIG. 28. Energy in axial c.m. motion versus pump strength for various detunings between cyclotron frequency and TE_{115} eigenfrequency.

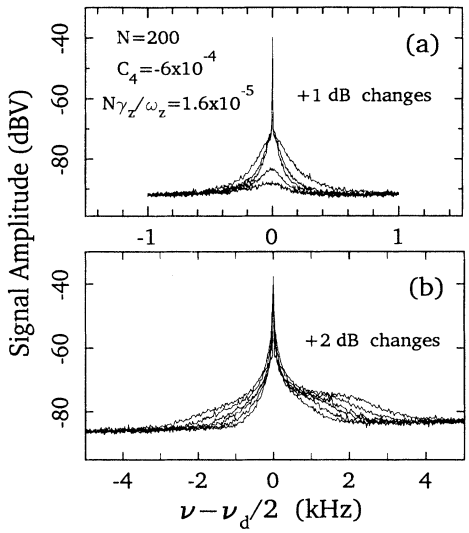

FIG. 29. Fourier spectra for various pump strengths. A sharp peak emerges as pump strength exceeds threshold (a), with only broadband spectrum appearing below threshold. Fluctuation spectrum continues to broaden with increasing pump strength (b), becoming skewed for very strong pumping.

for rigid motion. In spite of the disagreement, the observed line shapes (Fig. 10) agree qualitatively with the rigid model (Fig. 11). Taking a linear line shape such as in Fig. 10(a) as an example, the line shape is well preserved but the slope is observed to decrease when radiative cooling is reduced. The c.m. energy decreases also if the cyclotron oscillators are heated up with a microwave drive, as illustrated in Fig. 31.

The mechanism whereby the partially coherent c.m. motion becomes very sensitive to both cyclotron cooling and anharmonicity is not understood. It appears that individual electron oscillators may be excited to large amplitudes that are limited by anharmonicity and that the observed coherent response is generated by their synchronized component which would be strongly influenced by thermal processes involving energy exchange between

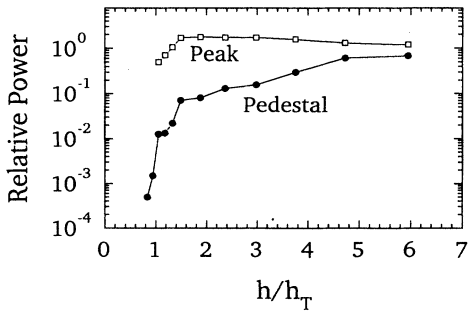

FIG. 30. Comparison of power in the peak (squares) with the integrated power in the fluctuation spectrum (circles) for the data set shown in the preceding figure.

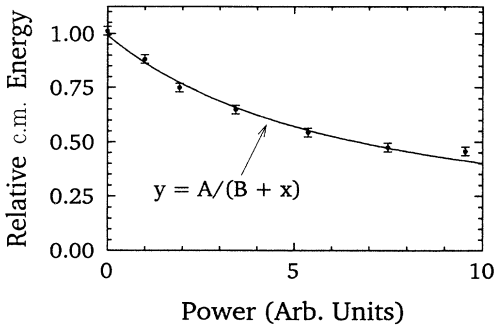

FIG. 31. Decrease in coherent response to parametric excitation when cyclotron motions are heated with a microwave drive. Measured energy in axial c.m. motion with parametric drive at lower corner frequency $\nu_d = \nu_-$ is plotted versus normalized microwave drive power (dots). A simple form (solid) fits well to it.

the axial and cyclotron motions. It is this sensitivity of the partially coherent c.m. motion to cooling of the internal motions [Fig. 28(a)] which has been very useful for probing the electron-cavity interactions (Fig. 14) so important for other radiative studies. We also find that the root-mean-squared (rms) saturation signal scales linearly with the number of electrons [Fig. 32(a)]. The rms signal below threshold is also consistent with a linear dependence on the number of electrons, but the slope is about 50 times smaller [Fig. 32(b)].

In contrast to the saturation and decline in power of the peak, we observe that the power in the fluctuation spectrum increases monotonically for $h < 6h_T$ (Fig. 30).

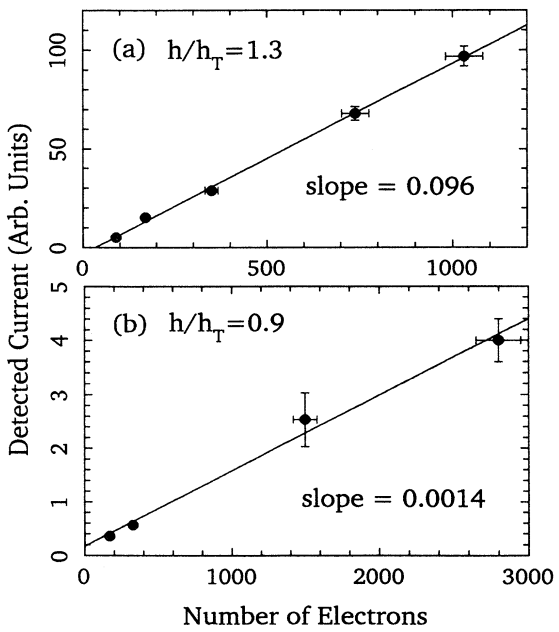

FIG. 32. Scaling of induced current with number of electrons (a) above threshold and (b) below threshold.

The rate of growth in fluctuation power decreases with pump strength. There are a few steplike structures where the fluctuation spectrum changes very little with incremental rise in pump strength, but more data are needed to confirm this and to improve the resolution. The powers in the peak and pedestal are converging for $h < 6h_T$. It is not known if this convergence continues for higher pump strengths which we have not yet been able to probe experimentally.

A parametric drive excites not only the collective, c.m. motion of N electron oscillators but also internal degrees of freedom. Even for small systems (< 100 electrons), the full dynamics is difficult to analyze. In the past, a "bolometric" model [20] was developed for the disordered, thermal motions of trapped electrons or ions and a simplified set of rate equations was thoroughly tested in experiments with electrons at $T \sim 80$ K [20]. In those early experiments, pulsed excitation showed that internal degrees of freedom come into thermal equilibrium so fast that they essentially form a single reservoir, with equilibration time shorter than other relaxation times. Since our apparatus is submerged in liquid He, simplifying assumptions used in earlier studies may not apply at the lower temperatures. A few pulsed excitation experiments were carried out in our apparatus. For example, Fig. 33(a) shows the response when electrons initially at 4 K are heated with a parametric drive below threshold in periodic 10-ms pulses. A storage oscilloscope captures the

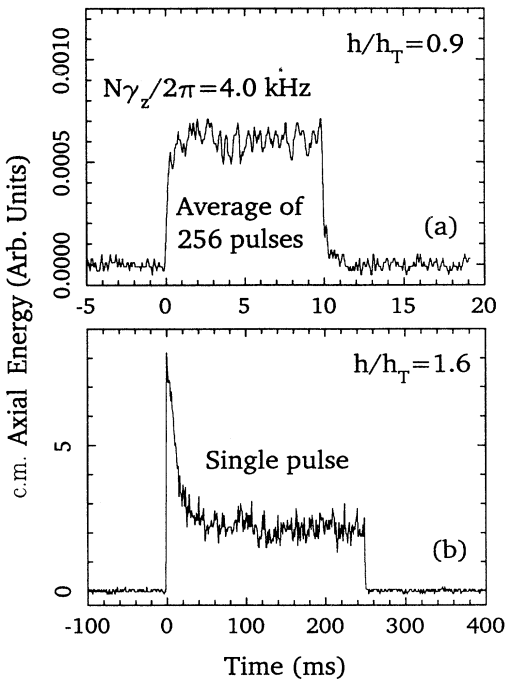

FIG. 33. Characteristic responses to pulsed parametric pumping (a) below threshold and (b) above threshold. Averaging over 256 pulses improves the S/N ratio (a) below threshold, but the response from a single pulse is easily observed (b) above threshold. Slow relaxation (b) follows intial rapid growth, above threshold.

response from each pulse and gives an output averaged over 256 pulses to improve the signal-to-noise ratio. Figure 33(a) shows the smooth relaxation which is characteristic of the response in a bolometric model [20] and, as expected, relaxation time is observed to be shorter when anharmonicity is increased ($|C_4|$ is made larger). This indicates that energy is transferred between internal reservoir and c.m. motion via the nonlinear couplings. However, when the pump strength is above threshold, new features are observed. Figure 33(b) shows the substantially larger response of the partially coherent response to a single 250-ms pump pulse above threshold. This response has a rapid initial growth overshooting the steady state, characteristic of parametric resonance discussed in Sec. III. Rapid growth stops abruptly and is followed by a much slower relaxation to a mean steady level with fluctuations. "Ring down" to the steady level (expected in rigid model, Fig. 7) is not observed, presumably being "washed out" by internal fluctuations. The slow relaxation to steady level is about 30 times longer than the typical rise time of the initial rapid growth or observed relaxation times below threshold. This new time constant does not seem very sensitive to changes in anharmonicity and pump strength, but this has not yet been studied in any detail. A more systematic study would extend over the full range of control parameters, including dependences on number of electrons and on detuning of cyclotron frequency from cavity-mode resonance, etc.

To see that Fig. 33(b) is a difficulty for a bolometric model, we now give a simplified set of rate equations describing energy transfer between axial c.m. motion and internal reservoir. Experimental evidence of its limitations follows. Below threshold, the bolometric model provides

$$C_z\dot{T}_z = -g_{z0}(T_z - T_0) + g_{iz}(T_i - T_z) + \dot{H}_z, \quad (16)$$

$$C_i\dot{T}_i = -g_{i0}(T_i - T_0) + g_{zi}(T_z - T_i) + \dot{H}_i, \quad (17)$$

where, for simplicity, the tuned circuit and cavity are assumed to be at the same temperature T_0. The axial c.m. oscillator has temperature T_z with heat capacity C_z. A reservoir formed from all internal oscillations has temperature T_i with heat capacity C_i. Damping of the c.m. motion due to a tuned circuit is characterized by conductivity g_{z0}. Internal motions decay to T_0 at a rate g_{i0}/C_i. Energy transfer between c.m. motion and the internal reservoir is characterized by conductivity $g_{iz} = g_{zi}$. For sufficiently high temperatures, the thermal conductivities g_{ij} and heat capacities C_i are approximately independent of temperature. A set of linear, first-order differential equations, such as Eqs. (16) and (17), cannot generate a response such as in Fig. 33(b).

Although this set of equations has been shown to be valid for temperatures above or near 80 K for weak pumping of trapped electrons [20], a more general system of equations would be necessary for electrons cooled to near liquid He temperature if the temperatures of the axial internal motions $T_{\|}$ and transverse internal motions $T_{\perp}$ do not equilibrate faster than other relaxation rates. Analysis of binary collisions in a strongly magnetized electron gas indicates a strong temperature dependence in this equilibration rate at very low temperatures, dropping rapidly as $T \longrightarrow 0$ [31–33]. In our study, pulsed cyclotron excitations show some evidence for this. In Fig. 34, the energy in the axial c.m. motion of $N = 1600$ electrons is monitored with a storage scope as a square wave activates a microwave drive to excite the cyclotron motions for 10 s, and then deactivates the drive for the next 10 s. The output is averaged over many drive cycles. (The parametric drive is disconnected.) If the equilibration rate is significantly smaller at lower temperature, then the rise time in the energy of the axial c.m. motion when cyclotron heating is turned on would be much longer than the decay time when heating is turned off. Observed relaxation is clearly non-exponential with the rise time significantly longer than the decay time, indicating a slower relaxation at low temperatures. As shown in Fig. 34, nearly 2 s after the microwave drive was applied, observed axial c.m. energy increased by less than 10%, but faster growth followed. In contrast, axial c.m. energy has dropped by over 80% within 2 s after the drive was turned off. More detailed experimental study near 4 K (at which 90% of cyclotron oscillators are in the ground state) may reveal other interesting features due to temperature-dependent collisional processes and may establish a generalized set of rate equations for low temperatures.

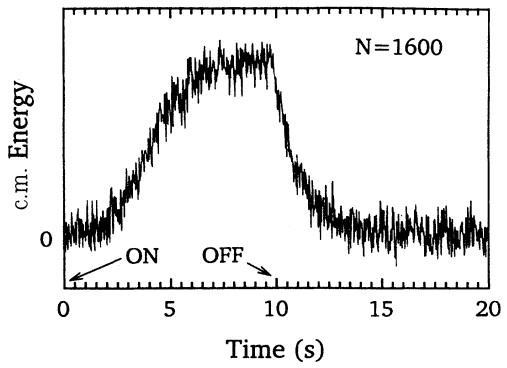

FIG. 34. Pulsed cyclotron excitation. Slow growth and fast decay in the axial c.m. energy indicates temperature dependence in the equilibration process.

VIII. CONCLUSIONS

A cylindrical Penning trap makes it possible to study both a single trapped electron and the nonlinear dynamics of parametrically pumped electrons. Anywhere between 1 and 10^5 electron oscillators can be isolated near the center of this trap cavity, localized in the simple standing-wave patterns of the radiation field which is excited by the motion of the electrons. Measured radiation mode frequencies agree very well with those calculated for an ideal cylindrical cavity, making it possible to identify the standing wave patterns in a trap cavity.

Many observed features are consistent with a simple model wherein the parametrically pumped electrons oscillate rigidly. The oscillators center-of-mass responds weakly and stochastically until the pump strength is in-

creased through a sharp theshold. Above the threshold, a strong response is observed which is coherent with the parametric pump. Resonance line shapes change as expected when the anharmonicity of the electron oscillators is varied.

Many other observed features cannot yet be accounted for by any simple model. The axial response not only depends upon coupling of electron cyclotron motion to a radiation mode of the trap cavity, but it does so in a way that produces Lorentzian line shapes. The center of mass of the electron oscillators abruptly makes nearly random transitions between degenerate response states which differ in phase by 180°. This collective behavior is self-organized insofar as the transition rate increases with increasing energy in the electron's internal motions. Observations on shorter time scales reveal a variety of phase jump "trajectories." Hysteresis is observed when either the strength or the frequency of the parametric pump is changed. Above the threshold, the stochastic component of the response grows with increasing pump strength.

The underlying simplicity of the many observed features (Lorentzian line shapes, exponential distribution of residence times, etc.) will hopefully prompt theoretical studies of this new nonlinear oscillator system. To this end, the dependences of the observation upon the system parameters are presented. System parameters such as the number of electrons, oscillator anharmonicity and damping, parametric pump strength and frequency, magnetic field, etc. are all under precise control. It should be possible in the future to study the onset of collective behavior as electron oscillators are added one at a time.

The first-time identification of radiation modes of a trap cavity is an initial application. A new generation of measurements of the electron's magnetic moment should be possible that are not limited by either cavity shifts of measured frequencies or by the broad damping linewidths which occur in free space. A thousand-fold decrease in an electron's axial temperature also seems feasible with the microwave field in the trap cavity under precise control.

ACKNOWLEDGMENTS

We are grateful to C. H. Tseng for experimental support. This research was supported by the Office of Naval Research and the National Science Foundation.

APPENDIX

A thorough analysis of coupled, parametrically pumped electron oscillators is not yet available, but this system is so well characterized that the full equations of motions of N electrons coupled to one cavity mode can be written down. The wide range of experimental control over system parameters allows some simplifications to be made. The kth electron has three degrees of freedom $\mathbf{r}_k = (x_k, y_k, z_k)$, which are made dimensionless by scaling to the size of the trap d. The coupled oscillations parallel to the symmetry axis of the trap (or to the magnetic field) satisfy

$$\ddot{z}_k + \gamma_z \sum_{i=1}^{N} \dot{z}_i + \omega_z^2 z_k + \tilde{C}_4 \omega_z^2 (2z_k^2 - 3\rho_k^2) z_k + \tilde{C}_6 \omega_z^2 (3z_k^4 - 15 z_k^2 \rho_k^4 + \tfrac{45}{8}\rho_k^4) z_k = \omega_{ee}^2 \sum_{\substack{i=1 \\ i\neq k}}^{N} \frac{(z_k - z_i)}{|\mathbf{r}_{ik}|^3} . \quad \text{(A1)}$$

Terms with coefficients $\tilde{C}_4$ and $\tilde{C}_6$ are due to deviations from an electric quadrupole potential. The series on the right-hand side describes the interparticle Coulomb repulsion. We assume that the axial frequency ω_z is tuned into resonance with a detection (LCR) circuit [5] so that the damping term, proportional to the center-of-mass velocity, accounts for the energy dissipation in the resistor representing the detection circuit.

For the (transverse) motions in the xy plane, we have

$$\ddot{x}_k - \omega_c \dot{y}_k - \frac{1}{2}\omega_z^2 x_k - 3\tilde{C}_4 \omega_z^2 (z_k^2 - \rho_k^2/4) x_k - \frac{15}{2}\tilde{C}_6 \omega_z^2 (z_k^4 - \tfrac{3}{2} z_k^2 \rho_k^2 + \tfrac{1}{8}\rho_k^4) x_k + \sqrt{\frac{r_e}{z_0}}\, \omega_M \Lambda_M(\mathbf{r}_k) \dot{f}_x = \omega_{ee}^2 \sum_{\substack{i=1 \\ i\neq k}}^{N} \frac{(x_k - x_i)}{|\mathbf{r}_{ik}|^3} , \quad \text{(A2)}$$

where $\mathbf{r}_{ik} = \mathbf{r}_i - \mathbf{r}_k$ and $\rho_k^2 = x_k^2 + y_k^2$; and

$$\ddot{y}_k + \omega_c \dot{x}_k - \frac{1}{2}\omega_z^2 y_k - 3\tilde{C}_4 \omega_z^2 (z_k^2 - \rho_k^2/4) y_k - \frac{15}{2}\tilde{C}_6 \omega_z^2 (z_k^4 - \tfrac{3}{2} z_k^2 \rho_k^2 + \tfrac{1}{8}\rho_k^4) y_k + \sqrt{\frac{r_e}{z_0}}\, \omega_M \Lambda_M(\mathbf{r}_k) \dot{f}_y = \omega_{ee}^2 \sum_{i\neq k}^{N} \frac{(y_k - y_i)}{|\mathbf{r}_{ik}|^3} . \quad \text{(A3)}$$

Coupling terms due to anharmonicity and Coulomb interaction are similar to those for the axial motions. Analogous to interaction between axial oscillator and a tuned circuit, the cyclotron oscillations are coupled to a standing-wave mode of the cavity. For simplicity, we have assumed the electrons are interacting with an $m = 1$ cavity mode near the trap symmetry axis. Then the dimensionless field components (f_x, f_y) near the trap center are governed by [24]

$$\begin{pmatrix} \ddot{f}_x \\ \ddot{f}_y \end{pmatrix} + \Gamma_M \begin{pmatrix} \dot{f}_x \\ \dot{f}_y \end{pmatrix} + \omega_M^2 \begin{pmatrix} f_x \\ f_y \end{pmatrix} - \sqrt{\frac{r_e}{z_0}}\, \omega_M \sum_{k=1}^{N} \Lambda_M(\mathbf{r}_k) \begin{pmatrix} \dot{x}_k \\ \dot{y}_k \end{pmatrix} = 0, \quad \text{(A4)}$$

where $\sqrt{r_e/z_0} = 8.56 \times 10^{-7}$. The couplings Λ_M are

TABLE I. Typical values of frequency parameters in the equations of motion.

Axial damping width	$\gamma_z/(2\pi)$	5 Hz (max.)
Collision constant	$\omega_{ee}/(2\pi)$	12×10^3 Hz
Axial frequency	$\omega_z/(2\pi)$	63×10^6 Hz
Cyclotron frequency (swept)	$\omega_c/(2\pi)$	$\sim 100 \times 10^9$ Hz

TABLE II. Parameters for two modes of experimental interest.

	TE_{115}	TE_{132}
Λ_M	0.31	0.56
$\Gamma_M/(2\pi)$	144×10^6 Hz	3.8×10^6 Hz
$\omega_M/(2\pi)$	99.513×10^9 Hz	97.525×10^9 Hz

related to those calculated and tabulated for regular geometries of interest [24]. The typical values of frequencies in these equations are provided in Table I.

The standing-wave configurations in a cylindrical cavity are described by known analytic functions, allowing us to characterize the electron-cavity coupling by the simple functions $\Lambda_M(\mathbf{r}_k)$. For the modes of greatest interest, near the trap symmetry axis, the electron-cavity coupling is given by

$$\Lambda_{1np}(\mathbf{r}_k) = \Lambda_{1np} \sin\left(\frac{p\pi d}{2z_0} z_k + \frac{p\pi}{2}\right). \tag{A5}$$

The first of two important cases is for an antinode at the midplane, e.g., TE_{115}, with

$$\Lambda_{115}(\mathbf{r}_k) = \Lambda_{115} \cos\left(\frac{5\pi d}{2z_0} z_k\right). \tag{A6}$$

For a small axial oscillation amplitude, the electron-cavity coupling is a simple constant in this case. The other important case produces cavity-mode resonances of a different type, namely the case for a node at the midplane, e.g., TE_{132}, with

$$\Lambda_{132}(\mathbf{r}_k) = -\Lambda_{132} \sin\left(\frac{\pi d}{z_0} z_k\right). \tag{A7}$$

For our apparatus, $d/z_0 = 0.923$. To facilitate calculation of examples that are of experimental interest, we provide sample values in Table II.

The system is parametrically excited by modulating the axial spring constant $m\omega_z^2$, so that the above equations are modified by the substitution

$$\omega_z^2 \longrightarrow \omega_z^2 [1 + h\cos(\omega_d t)]. \tag{A8}$$

The observed signal, obtained from the voltage induced across the effective detection resistor R

$$V = -\frac{1}{2}\kappa N q \left(\frac{d}{z_0}\right) \dot{Z}, \tag{A9}$$

is proportional to the axial velocity of the c.m.

$$\dot{Z} = \frac{1}{N}\sum_{i=1}^{N} \dot{z}_i. \tag{A10}$$

A phase-sensitive detector (as illustrated in Fig. 5) monitors the phase of the coherent response with respect to the pump. For c.m. energy measurements, this signal is amplified, squared, and filtered, giving an output proportional to $\langle \dot{Z}^2 \rangle$.

[1] J. Tan and G. Gabrielse, Phys. Rev. Lett. **67**, 3090 (1991).
[2] G. Gabrielse and F.C. MacKintosh, Int. J. Mass Spectrom. Ion Proc. **57**, 1 (1984).
[3] J. Tan and G. Gabrielse, Appl. Phys. Lett. **55**, 2144 (1989).
[4] G. Gabrielse and J. Tan, in *Cavity QED*, edited by P. Berman (Academic, New York, 1993), pp. 267–299.
[5] J. Tan, Ph.D. thesis, Harvard University, 1992.
[6] H. Haken, Rev. Mod. Phys. **47**, 67 (1975).
[7] V. Degiorgio, Phys. Today, **29** (10), 42 (1976).
[8] J.B. Hansen and P.E. Lindelof, Rev. Mod. Phys. **56**, 431 (1984).
[9] K. Wiesenfeld and P. Hadley, Phys. Rev. Lett. **62**, 1335 (1989); L. Fabiny and K. Wiesenfeld, Phys. Rev. A **43**, 2640 (1991).
[10] Y. Yamaguchi and H. Shimizu, Physica **11D**, 212 (1984).
[11] Y. Kuramoto and I. Nishikawa, J. Stat. Phys. **49**, 569 (1987).
[12] E. Niebur, H.G. Schuster, and D.M. Kammen, Phys. Rev. Lett. **67**, 2753 (1991).
[13] P.C. Matthews and S.H. Strogatz, Phys. Rev. Lett. **65**, 1701 (1990).
[14] S.H. Strogatz and R.E. Mirollo, J. Phys. A **21**, L699 (1988).
[15] H. Daido, Phys. Rev. Lett. **61**, 231 (1988).
[16] G. Nicolis and I. Prigogine, *Self-Organization in Nonequilibrium Systems* (Wiley, New York, 1977).
[17] See, for example, J.D. Jackson, *Classical Electrodynamics*, 2nd ed. (Wiley, New York, 1975), pp. 353–356.
[18] See review by L.S. Brown and G. Gabrielse, Rev. Mod. Phys. **58**, 233 (1986).
[19] D. Wineland, P. Ekstrom, and H.G. Dehmelt, Phys. Rev. Lett. **31**, 1279 (1973).
[20] H.G. Dehmelt and F.L. Walls, Phys. Rev. Lett. **21**, 127 (1968); D. Wineland and H. Dehmelt, J. Appl. Phys. **46**, 919 (1975).
[21] R.S. Van Dyck, Jr., F.L. Moore, D.L. Farnham, P.B. Schwinberg, and H.G. Dehmelt, Phys. Rev. A **36**, 3455 (1987).
[22] N.H. Nayfeh and D.T. Mook, *Nonlinear Oscillations* (Wiley, New York, 1979), pp. 338–348; L.D. Landau and E.M. Lifshitz, *Mechanics* (Pergamon, New York, 1976).
[23] R.S. Van Dyck, Jr., P.B. Schwinberg, and H.G. Dehmelt, Phys. Rev. Lett. **59**, 26 (1987).
[24] L.S. Brown, G. Gabrielse, K. Helmerson, and J. Tan,

Phys. Rev. Lett. **55**, 44 (1985); Phys. Rev. A **32**, 3204 (1985); G. Gabrielse, J. Tan, and L.S. Brown, in *Quantum Electrodynamics*, edited by T. Kinoshita (World, Singapore, 1990), pp. 389ff.

[25] G. Gabrielse and H.G. Dehmelt, Phys. Rev. Lett. **55**, 67 (1985).

[26] D. Wineland and H. Dehmelt, Int. J. Mass Spectrom. Ion Phys. **16**, 338 (1975); **19**, 251(E) (1975).

[27] G. Gabrielse, p. 631 in *Laser Manipulation of Atoms and Ions*, edited by E. Arimondo, W. Phillips, and F. Strumia (North-Holland, New York, 1992).

[28] M.G. Raizen, R.J. Thompson, R.J. Brecha, H.J. Kimble, and H.J. Carmichael, Phys. Rev. Lett. **63**, 240 (1989).

[29] Y. Zhu, D.J. Gauthier, S.E. Morin, Qilin Wu, H.J. Carmichael, and T.W. Mossberg, Phys. Rev. Lett. **64**, 2499 (1990).

[30] G. Gabrielse, X. Fei, L.A. Orozco, R.L. Tjoelker, J. Haas, H. Kalinowsky, T.A. Trainor, and W. Kells, Phys. Rev. Lett. **65**, 1317 (1990).

[31] T.M. O'Neil and P.G. Hjorth, Phys. Fluid **28**, 3241 (1985).

[32] T.M. O'Neil, Phys. Fluids **23**, 725 (1980).

[33] J.H. Malmberg and T.M. O'Neil, Phys. Rev. Lett. **39**, 1333 (1977).